Inverse models of gravity data from the Red Sea-Aden-East African rifts triple junction zone

Cynthia Ebinger, Valérie Ballu, Graham Stuart, Befekadu Oluma, Christel Tiberi

Geophys. J. Int. (2005) **163,** 775–787 doi: 10.1111/j.1365-246X.2005.02736.x

Inverse models of gravity data from the Red Sea–Aden–East African rifts triple junction zone

Christel Tiberi,[1]* Cynthia Ebinger,[1] Valérie Ballu,[2] Graham Stuart[3] and Befekadu Oluma[4]

[1]*Department of Geology, Royal Holloway University of London, Egham* TW20 0EX*, UK*
[2]*Laboratoire de Gravimètrie et Géodynamique, Institut de Physique du Globe, Case* 89, 4 *place Jussieu, Paris* 75252*, Cedex* 05*, France*
[3]*School of Earth Sciences, University of Leeds, Leeds* LS2 9JT*, UK*
[4]*Geological Survey of Ethiopia, Geophysics Department, Addis Ababa, Ethiopia*

Accepted 2005 July 4. Received 2005 June 29; in original form 2004 October 22

SUMMARY

The combined effects of stretching and magmatism permanently modify crustal structure in continental rifts and volcanic passive margins. The Red Sea–Gulf of Aden–Ethiopian rift triple junction zone provides a unique opportunity to examine incipient volcanic margin formation above or near an asthenospheric upwelling. We use gravity inversions and forward modelling to examine lateral variations in crust and upper mantle structure across the Oligocene flood basalt province, which has subsequently been extended to form the Red Sea, Gulf of Aden and Main Ethiopian rifts. We constrain and test the obtained models with new and existing seismic estimates of crustal thickness. In particular, we predict crustal thickness across the uplifted plateaux and rift valleys, and calibrate our results with recent receiver function analyses. We discuss the results together with a 3-D distribution of density contrasts in terms of magmatic margin structure. The main conclusions are: (1) a denser (+240 kg m^{-3}) and/or a thinner crust (23 km) in the triple junction zone of the Afar depression; (2) a shallower Moho is found along the Main Ethiopian rift axis, with crustal thickness values decreasing from 32–33 km in the south to 24 km beneath the southern Afar depression; (3) thicker crust (∼40 km) is present beneath the broad uplifted Oligocene flood basalt province, suggesting that crustal underplating compensates most of the plateau uplift and (4) possible magmatic underplating or a segmentation in the rift structure is observed at ∼8°N, 39°W beneath several collapsed caldera complexes. These results indicate that magmatism has profoundly changed crustal structure throughout the flood basalt province.

Key words: crustal thickness, density distribution, gravity inversion, magmatism, triple junction zone.

INTRODUCTION

The majority of passive margins worldwide are classified as 'magmatic margins' based on the characteristics of thick sequences of extrusive volcanic rocks extruded prior to or during rifting, and evidence for crustal underplating (e.g. Coffin & Eldholm 1994; Menzies *et al.* 2002). The large volumes of erupted basaltic material require elevated mantle temperatures, indicating that magmatic margins formed above or near mantle plumes (e.g. White & McKenzie 1989) or upper mantle convective upwellings (e.g. King & Anderson 1998). Despite the predominance of magmatic margins, there is no consensus on the nature of crust underlying the thick, riftward-dipping volcanic sequences, nor on the location of the ocean–continent boundary (e.g. Korenaga *et al.* 2000; Menzies *et al.* 2002). Studies of ancient passive margins provide only a partial picture of transitional continental crust because:

(1) the boundary is difficult to image beneath thick, seaward-dipping volcanic sequences that accumulate prior to or immediately after breakup (e.g. Holbrook & Kelemen 1993; Boutilier & Keen 1999) and

(2) the velocity contrast between more felsic continental crust and basic oceanic crust is less clear along magmatic margins owing to the dyke and sill emplacement during rifting (e.g. Cox 1980; Ebinger & Casey 2001). Likewise, little is known of the modification of crust and mantle lithosphere by plume processes during the late syn-rift stages (e.g. Buck 2004).

An alternative approach to studies of the continental breakup process is to probe lithospheric structure along incipient magmatic

*Now at: Université Pierre et Marie Curie-Paris 6, Laboratoire de Tectonique-CNRS/UMR 7072 4 place jussieu, 75252 Paris, Cedex 05 France. E-mail: christel.tiberi@lgs.jussieu.fr

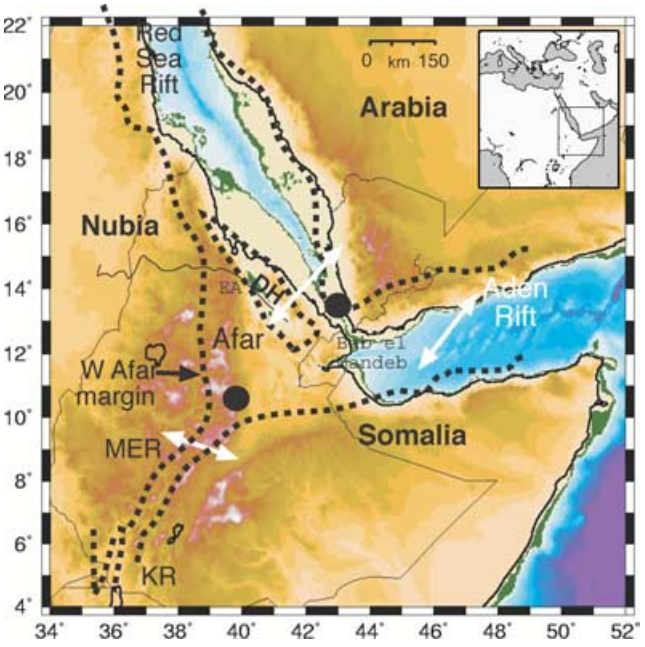

Figure 1. Tectonic setting of the southern Red Sea, Aden and Main Ethiopian rifts and their junction in the Afar depression. Bold dashed lines outline margins of rift valleys. DH is Danakil horst; MER is Main Ethiopian rift; KR is Kenya or Eastern rift. Arrows indicate extension directions. Pre-rift configuration crudely indicated by overlaying two large dots (after Wolfenden *et al.* 2004).

margins prior to the modifying effects of post-rift sedimentation, erosion of the uplifted rift flanks and thermal decay. The uplifted Ethiopia–Yemen flood basalt province, which includes the Afar triple junction, represents one such area (Fig. 1). The three arms of the Red Sea–Gulf of Aden–Main Ethiopian rift triple junction show diversity in structure and evolution; the southern Red Sea rift and western Gulf of Aden rifts comprise successfully rifted and incipient magmatic margins (e.g. Manighetti *et al.* 1997; Ghebreab & Talbot 2000), and the northern Main Ethiopian rift (MER) comprises highly evolved continental rifts and incipient seafloor spreading (e.g. Ebinger & Casey 2001; Keranen *et al.* 2004). Receiver function, tomography and seismic refraction studies of the Ethiopian plateau and rift valleys all suggest that large volumes of magmatic material have been added to the crust, but the lateral extent of these intrusions and underplate remains unclear (Keranen *et al.* 2004; Wolfenden *et al.* 2004; Dugda *et al.* 2005; Kendall *et al.* 2005; Mackenzie *et al.* 2005). Similarly, the compositions of rhyolites erupted from the Oligocene flood basalt episode to Pliocene time show increasing amounts of crustal contamination, indicating modification of the crust by magmatic processes (Ayalew & Yirgu 2003; Ayalew *et al.* 2005).

In this study we use a new compilation of gravity data from northeastern Africa to study modification of crust by tectonic and magmatic processes. We apply gravity data inversion methods and forward models to examine lateral variations in crust and upper mantle structure across this Cenozoic flood basalt province and superposed triple junction zone, testing models with new and existing seismic estimates of crustal thickness (Mechie & Prodehl 1988; Maguire *et al.* 2003; Dugda *et al.* 2005; Mackenzie *et al.* 2005). Gravity data compiled from northeastern Africa provide the regional perspective needed to evaluate lateral variations in crust and upper mantle structure within the triple junction zone (Oldenburg 1974). We then directly invert gravity data for lateral variations in density at specific depth levels (e.g. Widiwijayanti *et al.* 2004). The integrated results of the study are presented in a forward model of crustal structure along a rift-axis profile, which can explain available geological and geophysical data from the Main Ethiopian rift. Integrating our results with existing geophysical, geological and geochemical data from the region, we assess the role of magmatic modification of continental lithosphere during and after breakup.

GRAVITY AND TOPOGRAPHY DATA

A compilation of onshore and offshore gravity data from open file sources described in Ebinger & Hayward (1996), as well as gravity data acquired by the Geological Survey of Ethiopia during the period 1994–2001 are used in this study. All data are referenced to IGSN station values, but information on terrain corrections is not always available.

The merged data set contains a number of data of various vintages, and with varying height controls. We examined data in regions of closed contours of amplitude greater than 10 mGals, and deleted these values if there were no comparable values within <5 km. The resulting map shows many small-scale anomalies around geothermal prospects within the MER where data coverage is best. Hence, many of the shortest wavelength variations occur in Quaternary lava fields and eruptive centres (e.g. Mahatsente *et al.* 1999). Prior to spectral analyses, all gravity and topography data were transformed to UTM coordinates and then gridded with a 5-km-grid cell spacing (Figs 2 and 3).

TECTONIC PROVINCES

The Ethiopia–Yemen plateaux and flood basalt provinces have long been proposed as the expression of a mantle plume, and recent studies support this model (e.g. Courtillot *et al.* 2003; Montelli *et al.* 2004). A synthesis of $^{40}Ar/^{39}Ar$ data shows that up to 2 km of flood basalts and rhyolites were erupted throughout the southernmost Red

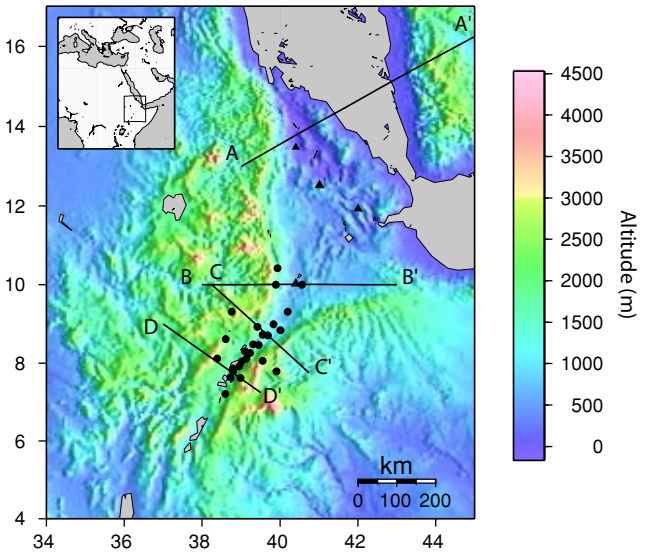

Figure 2. Topographic relief showing broad uplifted Ethiopian plateau (data from Gtopo30). Circles indicate seismological stations used to constrain forward model of Bouguer gravity anomalies designed to test inversion results (Fig. 6). Triangles mark midpoints of seismic refraction profiles described in Berckhemer *et al.* (1975) and Mechie & Prodehl (1988). Profiles AA′, BB′, CC′, DD′ of Figs 4(a)–(d) are shown by bold lines.

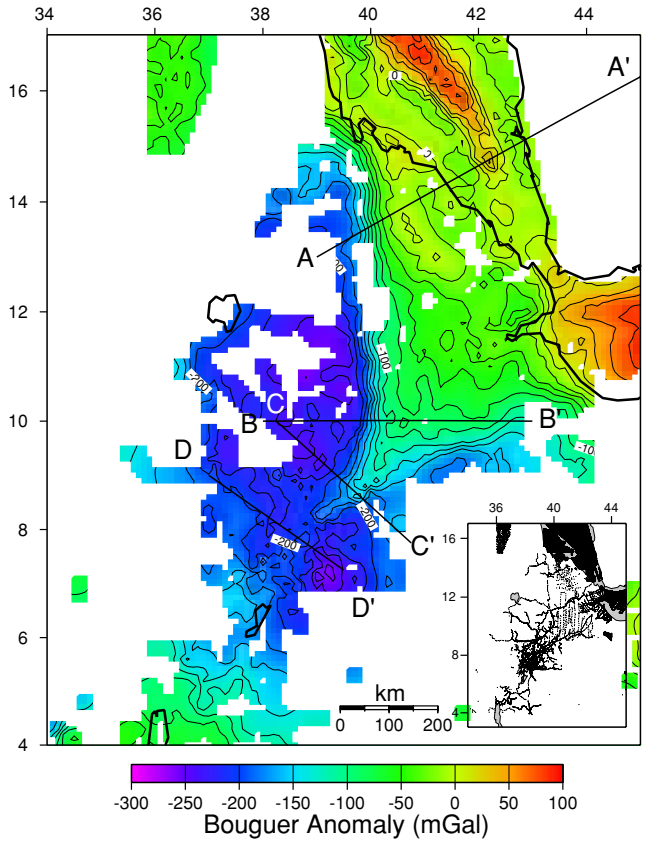

Figure 3. Bouguer gravity anomaly map. Bold lines indicate locations of profiles AA′, BB′, CC′ and DD′ of observed gravity, topography, and crustal thickness predicted from 3-D gravity inversion (Figs 4a–d). Inset is the distribution of the gravity stations used to prepare the map. Data include unpublished values from the Geological Survey of Ethiopia, as well as the compilation used in Ebinger & Hayward (1996) and data from the Tadjouraden experiment (Hébert *et al.* 2001).

Sea region at ∼31 Ma (e.g. Hofmann *et al.* 1997; Pik *et al.* 2003), although less widespread and possibly related volcanism affected SW Ethiopia at ∼40 Ma (e.g. Ebinger *et al.* 1993; George *et al.* 1998). The volcanic units overlying uplifted Mesozoic marine sequences now form a *ca.* 2500-m-high plateau on both sides of the southern Red Sea and western Gulf of Aden (Fig. 2).

The triple junction between the Red Sea, Gulf of Aden and the MER, the northernmost sector of the East African rift system, lies within the Afar depression west of the Danakil microplate (e.g. Manighetti *et al.* 1997; Tesfaye *et al.* 2003) (Fig. 1). The geographical position of plate boundaries, however, has changed considerably since initial rifting in the southern Red Sea and Gulf of Aden at ∼30 Ma (e.g. Tesfaye *et al.* 2003). Extension in the southernmost sector of the Red Sea, which terminates at ∼10°N, commenced concurrent with or immediately after the emplacement of thick, widespread rhyolites at ∼28 Ma (Wolfenden *et al.* 2005). Timing constraints in the Gulf of Aden are sparse, but extension had commenced by 30 Ma as Arabia and Africa began to separate (e.g. Cochran 1981; Bellahsen *et al.* 2003). Seafloor spreading in the eastern Gulf of Aden propagated toward the Afar depression since 18 Ma (e.g. Manighetti *et al.* 1997); seafloor spreading in parts of the Red Sea commenced at ∼4 Ma, with incipient seafloor spreading on the western (SW Red Sea) and east (SE Red Sea) of the Danakil microplate (Cochran 1983; Tesfaye *et al.* 2003) (Figs 1 and 2). WNW-directed extension within the third arm of the triple junction, the MER commenced at ∼18 Ma in southwestern Ethiopia, and propagated northward into the Afar depression after 11 Ma (WoldeGabriel *et al.* 1990; Wolfenden *et al.* 2004). Thus, the MER is a much younger, and less evolved, rift than the Red Sea and Gulf of Aden rifts, which it now cross-cuts.

Seismic data from the Ethiopian plateau region provide critical constraints on the depths to density contrasts within and below the plates. Tomographic models reveal low-velocity material within the upper mantle, but the relationship between this hot zone and the deep mantle low-velocity zones beneath southern Africa are debated (e.g. Ritsema & van Heijst 2000; Montelli *et al.* 2004). Hadiouche *et al.* (1989) and Knox *et al.* (1998) report anomalously low *S*-wave velocities in the upper mantle beneath Afar at depths of ∼60 and 130 km depth, implying the presence of partial melt, based on analyses of interstation Rayleigh and surface wave phase velocities between Addis Ababa and Djibouti. Higher resolution *P*- and *S*-wave tomography models indicate that mantle lithosphere is <40 km thick beneath the northern MER (Bastow *et al.* 2005), and upper mantle velocities are anomalously low beneath the southern part of Arabia (Benoit *et al.* 2003).

Below we discuss the main features of the Bouguer anomaly field, and summarize existing constraints on crust and upper mantle structure beneath each of the three rift arms and the uplifted plateau region (Figs 2–4).

Ethiopian plateau (Nubian plate) and Somalia plateau (Somalia plate)

The Ethiopian plateau is ∼1000 km wide, and has a mean elevation of ∼2500 m (Figs 2 and 4c). Much of the now elevated plateau lay below sea level through early Cretaceous time when ∼800 m of marine clastic and carbonate sequences were deposited (e.g. Bosellini *et al.* 2001). The Mesozoic marine sequences overlying Precambrian basement thicken to the southeast (Bosellini *et al.* 2001). The flood volcanic sequences above the Mesozoic strata reach 2 km near the present-day southern Red Sea rift (e.g. Wolfenden *et al.* 2005), but thin to <1 km to the west and south across the plateau (e.g. George *et al.* 1998; Kieffer *et al.* 2004).

Seismic refraction and receiver function data show crustal thicknesses of 35–44 km beneath the plateau south of Addis Ababa (Berckhemer *et al.* 1975; Hebert & Langston 1985; Ayele *et al.* 2004; Dugda *et al.* 2005) (Fig. 4c). Crustal thickness is slightly less (31–41 km) on the Somalia plateau, the southern side of the MER (Dugda *et al.* 2005; Mackenzie *et al.* 2005) (Fig. 4). Both plateaux are associated with long wavelength low amplitude Bouguer anomaly (*ca.* −250 mGal, Figs 3 and 4c and d). Woldetinsae & Götze (2005) analysed a similar gravity data base and found that most of the long-wavelength gravity signal could be explained by an Airy isostasy model, with a small component of dynamic support for the broad plateau uplift. Considering the gaps in data coverage and the presence of two or more mid-ocean ridges within the flood basalt province, we can add little new to the earlier studies of Ebinger *et al.* (1989) and Woldetinsae & Götze (2005) (Fig. 3).

Southwestern Red Sea

The southwestern Red Sea is the region of relatively positive Bouguer anomalies lying between the plateau and the Danakil horst, and lying north of 10°N (Figs 1 and 4a). This sector includes the ∼3000-m-high Western escarpment, which bounds the Oligocene Red Sea rift basins (Wolfenden *et al.* 2005) (Figs 1–3, 4a and b).

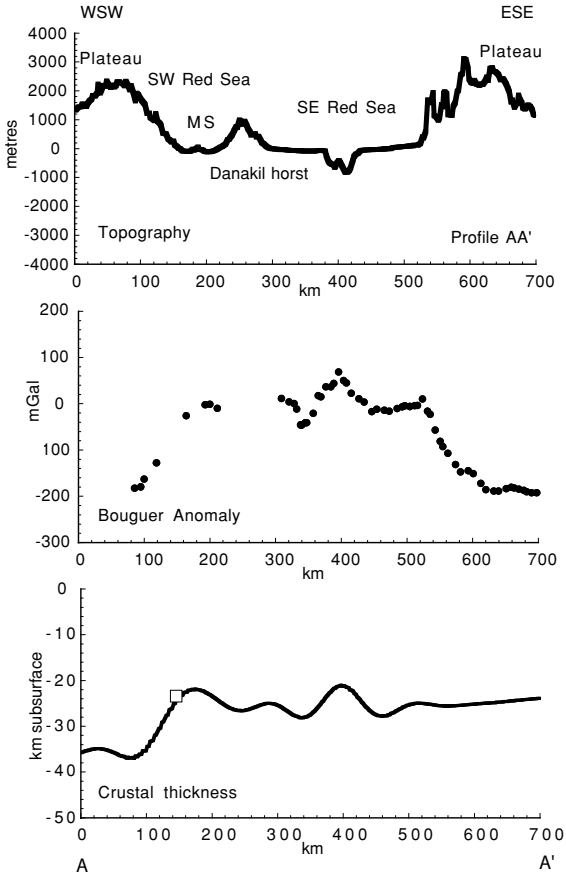

Figure 4. Profiles of topography, Bouguer gravity anomaly, and crustal thickness estimates obtained in the 3-D inversion of filtered Bouguer anomaly data (Fig. 6). Circles indicate depths estimated from receiver function studies; squares, estimates from refraction profiles. Locations of profiles shown in Figs 2 and 3. (a) AA′ transect of Ethiopian margin, Afar depression, Danakil horst, Red Sea, and Yemen margin. Note the very steep, symmetrical anomalies on marking both volcanic passive margins. (b) BB′ transect of Ethiopian plateau, uplifted flank to southern Red Sea, and superposed MER. The steep gradient corresponds to thick riftward-dipping sequences of basaltic lavas analogous to seaward-dipping reflector sequences (SDR) on magmatic margins worldwide (Wolfenden *et al.* 2004). (c) CC′ transect of northern Main Ethiopian rift showing southeastward decrease in plateau elevation. Maximum crustal thickness is predicted beneath the 2500 m-high plateau. (d) DD′ transect of central Main Ethiopian rift crossing the Butajira volcanic lineament and water-filled collapsed calderas. The eastern margin traverses the flank of Pliocene Chilalo volcano.

Topographic and structural transects of the margin show that the steep gravity gradient on the western margin corresponds to steeply dipping basaltic lavas analogous to seaward-dipping reflector sequences on passive continental margins (Wolfenden *et al.* 2005) (Figs 4a and b). The central depression (Danakil depression) is marked by the Quaternary 'axial volcanic ranges' of Barberi & Varet (1977) (Fig. 4a). The segmented axial ranges are aligned chains of primarily basaltic eruptive centres, characterized by segmented positive Bouguer anomalies (e.g. Hayward & Ebinger 1996) (Fig. 4a). The high heat flux and broad, low form of Erta 'Ale range led Oppenheimer & Francis (1997) to propose that new igneous crust is being formed by magmatic intrusion into the axial ranges (magmatic segments).

Previous teleseismic, seismic refraction, and gravity studies show an increase in crustal thinning from south to north in the Afar

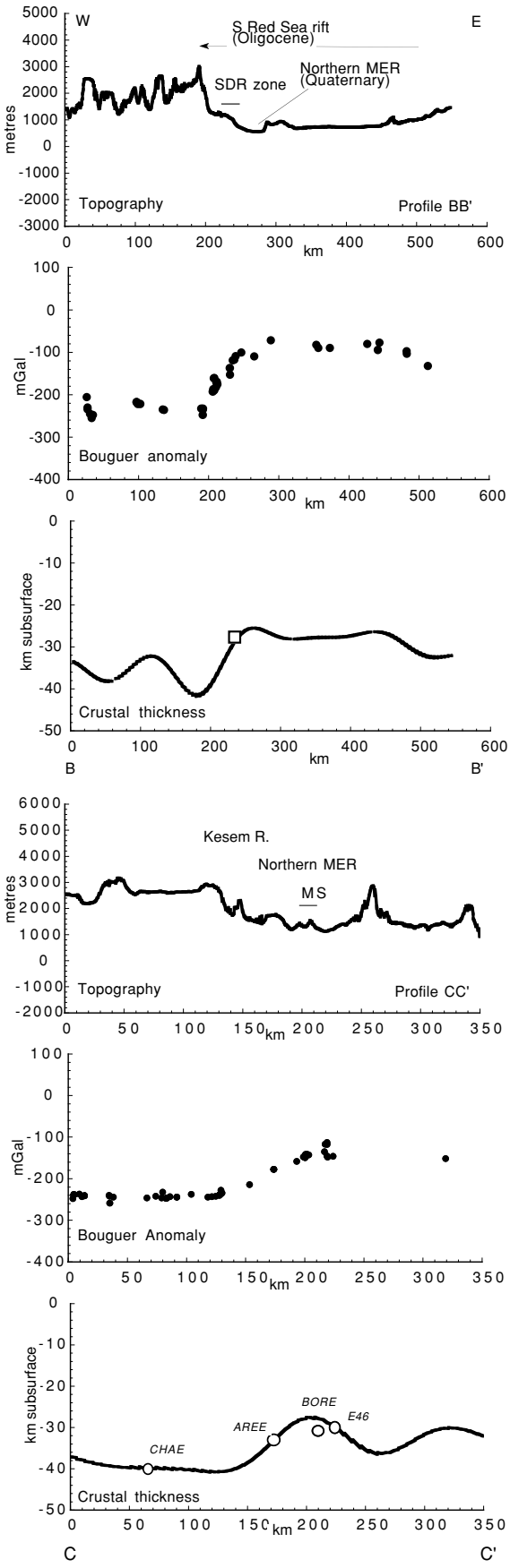

Figure 4 (*Continued.*)

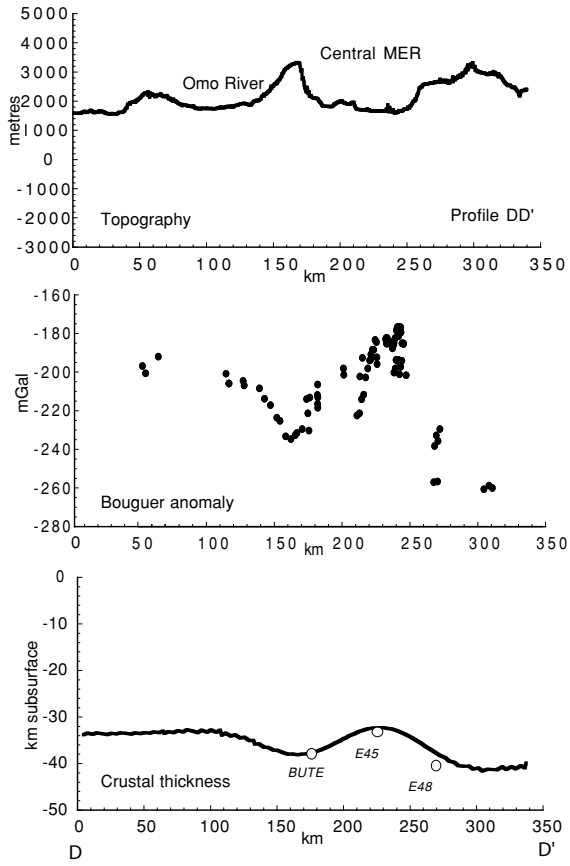

Figure 4 (*Continued.*)

depression. Refraction profiles in Afar suggest a 25-km thick mafic crust underlain by a 10-km thick layer with anomalously low upper mantle *P*-wave velocities above apparently normal mantle (Berckhemer *et al.* 1975; Mechie & Prodehl 1988) (Fig. 2). Makris & Ginzburg (1987) interpreted the seismic data and earlier Bouguer gravity compilations as hot upper mantle overlying more normal upper mantle at 45 km depth. New and existing refraction data reveal high-velocity intrusions into the lower crust, which rise to ∼8 km subsurface beneath the magmatic segments of the northernmost MER (Mechie & Prodehl 1988; Mohr 1989; Maguire *et al.* 2003). Thus, the crust has been extended and extensively modified by magmatism.

Western Gulf of Aden

Only a small portion of the Aden spreading ridge lies within our study area. The western Gulf of Aden spreading ridge continues westward into the Afar depression via the Gulf of Tadjourah, rather than connecting with the high-strain extensional province of the southeastern Red Sea via the Straits of Bab el Mandeb (Figs 1 and 2). Hébert *et al.* (2001) interpret a narrow zone of new oceanic lithosphere beneath the ridge axis between 44°–45°E.

Main Ethiopian Rift

The MER comprises Miocene–Recent rift basins whose degree of extension and magmatic modification increase to the north (Maguire *et al.* 2003), consistent with an along-axis decrease in effective elastic thickness and seismogenic layer thickness (e.g. Ebinger & Hayward 1996). In the northernmost MER a system of aligned Quaternary eruptive centres form an en echelon array within the rift valley (Ebinger & Casey 2001). These zones of magmatic construction and dyke injection, referred to as magmatic segments, are characterized by positive Bouguer anomalies that become increasingly more positive to the north (Figs 3 and 4c). Crustal tomography models show that the narrow magmatic segments are underlain by anomalously high-velocity material interpreted as cooled mafic intrusions (Keranen *et al.* 2004; Daly *et al.* 2005). Mahatsente *et al.* (1999) modelled the short-wavelength, positive Bouguer anomaly over the magmatic segments with a 20-km-wide zone of basaltic intrusion through the crust.

Seismic data acquired in 2001–2003 incorporate earlier studies by Berckhemer *et al.* (1975) and Mechie & Prodehl (1988) (Maguire *et al.* 2003; Dugda *et al.* 2005; Stuart *et al.* 2005). Crustal thickness is greatest (40–44 km) beneath the flanks of the rift, with greater thicknesses and higher mean velocities observed on the NW flank (>40 km) than on the eastern flank (<40 km) (Figs 4c and d). The ∼N–S trending gravity lineament at ∼40°E also corresponds to a contrast in crust and upper mantle velocity structure, suggesting a Precambrian terrane boundary underlies the flood volcanics (Stuart *et al.* 2005) (Fig. 3). Seismic refraction and receiver function data west of 40°E show a 7.4–7.7 km s^{-1} layer at ∼30 km depth, interpreted as mafic underplate probably accreted during the flood basalt event (Mackenzie *et al.* 2005).

Beneath the MER, crustal thickness decreases from south to north (Fig. 4). Moho is not well imaged in receiver function and refraction data beneath the ∼20 km-wide magmatic segments, suggesting the presence of partial melt in the upper mantle (Maguire *et al.* 2003; Stuart *et al.* 2005). There are, however, no measurements of crustal thickness south of 7°N. Thus, existing refraction and receiver function data suggest up to 25 per cent of the crust beneath the northern MER and Afar depression is new igneous material, but with minor amounts of crustal thinning south of Fantale volcano (∼9°N).

GRAVITY METHODS

It is well known that gravity inversion suffers from non-uniqueness of solutions emphasized by the discretization and inaccuracy of the sampled data set. It is then essential to derive realistic *a priori* information to reduce the number of possible models. Where geological and independent geophysical studies allow one to make the assumptions essential to obtain realistic models, one can extract *a priori* information from the gravity signal itself. We first used two different and independent methods of gravity inversion: the Oldenburg method and a 3-D inversion. The first one allows us to obtain the crustal thickness in the MER area. The second one allows us to localize in depth the distribution of density contrast, thereby mapping areas of magma intrusion and stretching imaged in sparser seismic data for the same area. Finally, to test our results, we forward model the gravity along the MER axis with constraints from existing receiver functions results. The following section deals with the methodologies we used, before we present the results.

Oldenburg inversion

The observed Bouguer gravity anomaly could come from mainly two different sources: the Moho topographic variations, and the crustal heterogeneities (e.g. mafic crust, volcanic intrusions, crustal thinning). The contribution by deeper sources should be small across our comparatively small study area with respect to the African

Superplume province (e.g. Ritsema & van Heijst 2000). We can make the assumption that short wavelengths are mainly the expression of small-scale crustal heterogeneities, whereas long wavelengths mostly result from relief on the Moho boundary. The presence of a 10–15 km thick underplate zone complicates, but does not prevent an inversion for crustal thickness. Firstly, subcrustal mantle velocity is ∼8.1 km s^{-1} except beneath the ∼20 km-wide magmatic segments where velocities are lower (Mackenzie *et al.* 2005; Maguire *et al.* 2003). Secondly, the presence of thick, high-velocity crustal layer reduces the density contrast at the Moho, but the underplate is not representative of the mean crustal density. Instead, a relatively high density contrast at the Moho is needed to account for the underplate (see below).

We separate the wavelengths by upward continuation of the signal to a horizontal plane 15 km above the plateau elevation. We then use the approach of Oldenburg (1974) to image crustal thickness variations throughout the Ethiopian plateau and triple junction zone.

This method is based on the direct formula of Parker (1972) that calculates the gravity signal of a 2-D uneven layer with a constant density:

$$F(\Delta g(x)) = -2\pi G \Delta\rho e^{-|k|z_0} \sum_{n=1}^{\infty} \frac{|k|^{n-1}}{n!} F(h^n(x)). \qquad (2)$$

Here F indicates the Fourier Transformation, Δg is the gravity signal, k is the wavenumber, x the horizontal coordinate, G is Newton's gravitational constant, z_0 is a reference depth, n is an integer and $\Delta\rho$ is the density contrast between the two media. The function $h(x)$ represents the topography of the interface. In this application, we sum to $n = 4$.

Oldenburg (1974) solved the inverse problem by an iterative approach, and thus he retrieved the layer's thickness from the gravity signal. The problem is typically non-unique and requires one to fix first a reference depth from which the topographic variation is calculated and second a constant density contrast between the two layers. The additional use of a cosine taper during the inversion helps the inversion to stabilize (Oldenburg 1974).

We use here a reference depth of 28 km, which represents a mean thickness for the broad Afar depression, rift valleys, and plateau areas, and a density contrast of 530 kg m^{-3} that corresponds to the difference between a crust of 2670 kg m^{-3} (value used for the Bouguer anomaly calculation) and a mantle of 3200 kg m^{-3}. Clearly, this density contrast is too high for areas of underplating and intense magmatic intrusion, and lateral variations in density will be mapped into variations of crustal thickness. Hence, a variety of density contrasts is tested against the available seismic data, as discussed below. We used a cosine taper between 70 and 170 km as advised by Oldenburg (1974). The gravity signal was mirrored to ease the work in the space domain, and to get rid of boundary effects.

The results are shown in Figs 5 and 6. Convergence was obtained after five iterations, with a final root mean square (rms) of 1.068 mGal, compared to the initial of 1.926 mGal. The gravity signal calculated from the resulting topography is extremely close to the initial one. The longest wavelengths are retrieved, and the residuals (Fig. 5c) only affect very small areas and present low amplitudes (±7 mGal), which is less than 5 per cent of the initial amplitude of the signal. The main features in Fig. 6 are located along the major tectonic structures identified at the surface: thin crust beneath the Danakil depression and along the rift axis in a N–S direction, and thicker crust outside the rift, beneath the uplifted plateau (Figs 5 and 6).

Of course, these are only relative results, because the amount of crustal thinning and thickening is strongly dependent on the choice of the reference depth and the density contrast (Oldenburg 1974). The deeper the reference, the greater the relative topography and the greater the density contrast, the smaller the relative topography. Moreover, this method does not take into account the lateral changes in the density contrast. Especially, in the case of mafic crust, the signal due to the increased mass of denser material increases, and these lateral density contrasts can explain a significant part of the gravity signal. The high observed Δg (Fig. 3) is partly coming from the mafic crust imaged in seismic data. What we account for in Oldenburg's inversion is only a density contrast at the Moho, but we require a higher density contrast to invert the entire signal (Christensen & Mooney 1995). Thus, we expect our results to overestimate the crustal thinning where the crust is believed to be more mafic, such as in the highly stretched and intruded Afar depression (Fig. 1).

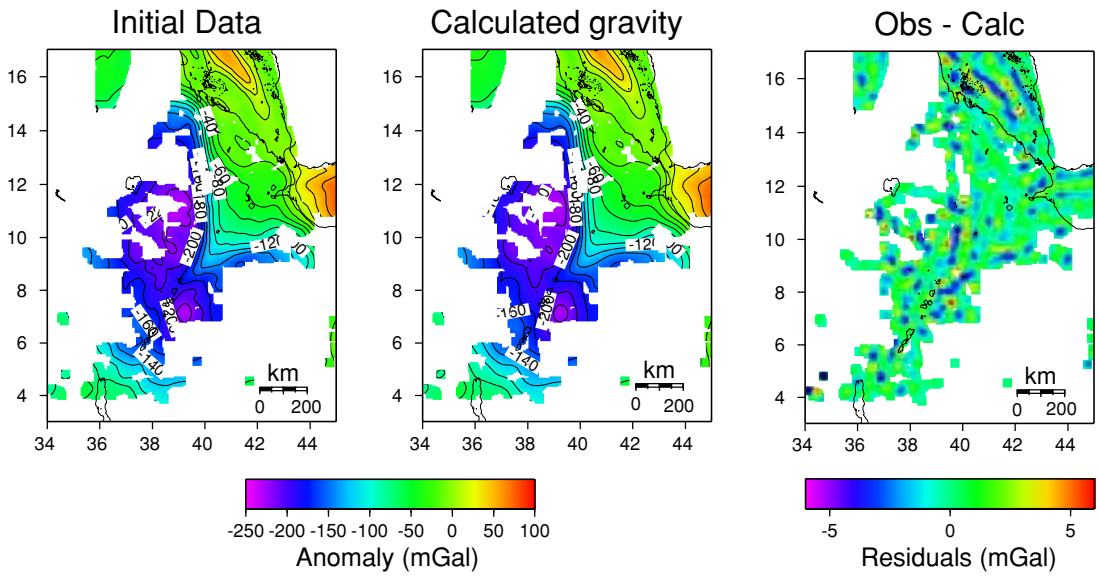

Figure 5. The initial gravity signal and the retrieved signal from Oldenburg inversion are shown in (a) and (b), respectively. (c) represents the residuals (observed–calculated). This comparison reveals few differences, and the principal features are very well retrieved.

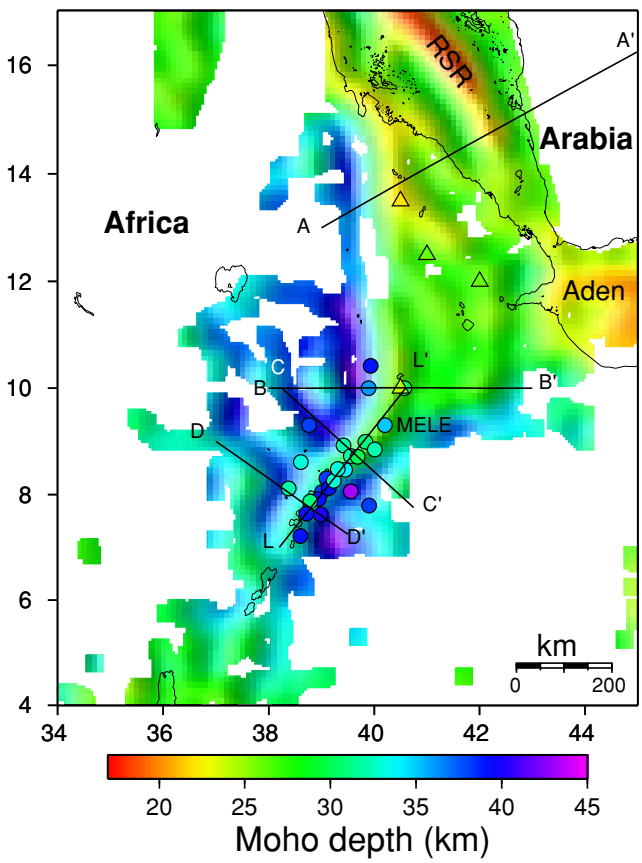

Figure 6. Topographic relief at the base of the crust obtained from the Oldenburg-type inversion. Estimates of crustal thickness from regional refraction profiles of Berckhemer *et al.* (1975) are shown in triangles with the colour scale representative of their value. Crustal thickness estimates from receiver functions are also shown with the circles (same colour scale than the Moho depth). Line LL′ marks longitudinal profile for forward model showing in Fig. 9. Station MELE has been noted for being more extensively discussed in the text.

Table 1 summarizes different tests we perform to illustrate the trade-off between $\Delta\rho$ and z_0. Our aim is not to provide a complete and exhaustive list of the different combinations of possible $(\Delta\rho, z_0)$ couples, but rather to show some relevant examples. The comparison is made with the receiver function of Stuart *et al.* (2005). To account for large Δg as observed, we can either chose moderate depth z_0 with high $\Delta\rho$ (Table 1, case ref.), or very shallow depth z_0 with moderate $\Delta\rho$ (Table 1, case 4). The first thing we observe is that upraising z_0 too much with moderate $\Delta\rho$ leads to unrealistic Moho depth values between 2 km and 38 km (Table 1, case 4). Second, when we take a lower density contrast, it induces unlikely large Moho depth variations for a reasonable range of z_0 (Table 1, case 1). So we finally are limited for the choice of $\Delta\rho$ and z_0. We investigate the case of a more likely value of $\Delta\rho$ ($= 400\,\mathrm{kg\,m^{-3}}$) with a slightly deeper z_0 ($=$ 30 km) in case 5, but the difference between the gravity results and the receiver function results is bigger than for the reference values (see e.g. the rms value in Table 1). We thus choose the density contrast to be $530\,\mathrm{kg\,m^{-3}}$, with the knowledge that this value is not representative of the density contrast at the Moho.

One way to test our results is to compare our crustal thickness estimates from Oldenburg's method with crustal thickness estimates from seismic studies (Figs 4 and 6) (Stuart *et al.* 2005; Dugda *et al.* 2005; Mackenzie *et al.* 2005; Maguire *et al.* 2003). A selection of the 80 receiver function estimates are reported in Fig. 6 and Table 2. Fig. 6 shows the depth of the interface compared with crustal thickness estimates from broadband stations of the

Table 2. Comparison between crustal thickness resulting from gravity inversion and from receiver function analysis (Stuart *et al.* 2005). The values from gravity modelling are those interpolated for the station locations represented on Figs (2)–(4) and 6.

Stations	Moho depth (km) from gravity	Moho depth (km) from seismology	*Vp*/*Vs* ratio
E32	28.4	32	1.9
E34	32.9	39	1.9
E45	32.9	33	1.9
E46	28.1	30	1.9
E47	30.9	34	1.9
E48	37.1	40	1.9
E53	33.1	38	1.9
E54	33.4	39	1.9
E63	32.5	33	1.9
E75	33.6	39	1.9
E77	32.7	31	1.9
E79	32.9	39	1.9
E80	30.1	33	1.9
ADEE	35.0	38	1.8
AMME	31.2	38	1.9
AREE	33.4	32	1.9
BORE	28.5	32	1.9
BUTE	37.4	32	2.0
CHAE	39.3	38	1.8
DIKE	38.6	43	1.9
GTFE	26.7	31	2.0
HIRE	36.1	39	1.8
LEME	35.4	33	2.0
MELE	26.5	35	2.1
SHEE	36.8	36	2.1
WANE	26.5	30	2.0

Table 1. Comparison between different inversions with parameters variations. We have changed the density contrast and the depth reference to estimate the variation in the resulting Moho depth. This estimation has been made by comparing the Moho depth obtained from the gravity inversion at the seismic stations locations with the one from the corresponding receiver functions (hereafter referred as mean difference). The values in bold represent the ones that have changed compared to the reference test.

Test	$\Delta\rho$ (g cm^{-3})	z_0 (km)	Min. max. Moho depth (km) from gravity inversion	Mean difference (km) with RF	Root mean square
Ref.	0.53	28	17.7/43.2 (diff. = 25.5)	2.57	3.28
1	**0.3**	28	11.6/59.6 (diff. = 48.0)	−0.66	5.91
2	**0.63**	28	19.2/40.4 (diff. = 21.2)	3.28	3.03
3	0.53	**30**	19.1/46.0 (diff. = 27.0)	0.67	3.42
4	**0.3**	**15**	1.9/37.9 (diff. = 36.0)	11.44	3.91
5	**0.4**	**30**	16.2/52.6 (diff. = 36.4)	−0.70	4.43

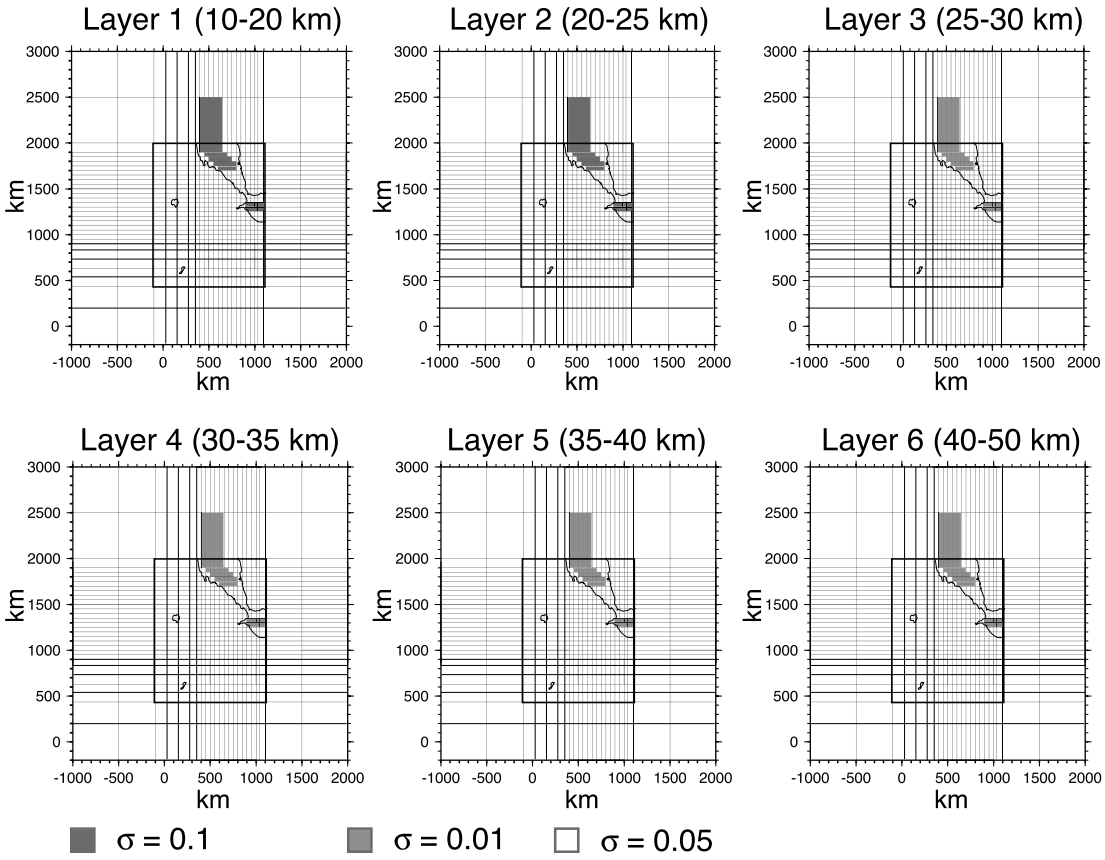

Figure 7. Parametrization for the initial model of the 3-D gravity inversion. The model is composed of six layers, each of them gridded into rectangular blocks shown by the light grey lines. The inside bold rectangle represents the area of data with coast lines indicated in thin black lines. We introduced *a priori* constraints by associated different standard errors to each blocks. Standard error is initially set to 0.05 in all blocks for every layer, except in two areas: the Red Sea and the Gulf of Aden. For these two locations, the two first layers have high standard errors (0.1, shown in black) whereas the deeper layers (3–6) show lower standard errors (0.01, light grey).

EAGLE passive array (Stuart *et al.* 2005) and Dugda *et al.* (2005). Thickness estimates were made by assuming an average velocity of 6.0 km s^{-1} (average crustal velocity from Mackenzie *et al.* 2005) and a varying Vp/Vs ratio between 1.8 and 2.1 (Table 2). The correlation between the Oldenburg inversion and the receiver function analysis is very good (Figs 4 and 6). Notably, we retrieve a shallow Moho at the rift axis with an average depth of about 27–30 km (e.g. stations E46, E77), and a thick crust at the edges with values ranging from 35 to more than 40 km (e.g. LEME, CHAE, DIKE, ADEE). One special attention should be drawn for the station MELE (Table 2). The receiver function result shows an interface at 35 km depth, that is 7 km more than the estimate from the refraction profile near MELE (28 km, Maguire *et al.* 2003). Thus our estimate from Oldenburg (∼27 km) coincides more with the refraction Moho at this location (Fig. 6).

3-D density model

To take into account the possible lateral changes in density contrast, we perform a 3-D gravity inversion. The aim of the inversion is to obtain a distribution of density variations in a 3-D model space that can fit the observed gravity data in a least-squares sense. The causative sources of the local complete Bouguer gravity anomaly are assumed to be distributed in N horizontal layers of thickness H_i, $i = 1, 2, \ldots, N$, in the upper lithosphere. Every layer is subdivided into a number of rectangular blocks in which an initially homogeneous density contrast is assigned (Fig. 7). The average density variation per layer is assumed to be zero, and the mean density contrast is subtracted after each iteration to maintain this condition in each layer. The final density contrasts retrieved by the inversion are then relative to each layer, and cannot be directly compared between depths.

The method we use is based on a Bayesian approach in which any *a priori* information can be introduced in order to reduce the set of possible solutions (e.g. Widiwijayanti *et al.* 2004). We invert the same data set as for the Oldenburg inversion (i.e. 15 km upward-continued, 4019 data). As a consequence, we neglect surficial density variations, and we start our model at 10 km depth. Six layers constitute the initial model down to 50 km depth. Each layer is equally divided into 50 × 50 km blocks in the central area, and with larger blocks on the edges (Fig. 7). We chose a more detailed gridding in the central part characterized by shorter wavelengths. The grid becomes cruder on the edges, first to be consistent with the data distribution, and second to widen the model to eliminate possible boundary effects (Fig. 7). No initial density variation is entered within the layer. We start the inversion with a homogeneous density contrast model. However, we enter *a priori* information via the standard deviation in two specific areas: the southern Red Sea and Aden spreading ridges. The standard deviation for all layers and blocks is set to 0.05, except in the Red Sea and Gulf of Aden areas, where it is set to 0.1 for layers 1 and 2, and 0.01 for layers 3 to 6, respectively (Fig. 7). By increasing the parameters' standard

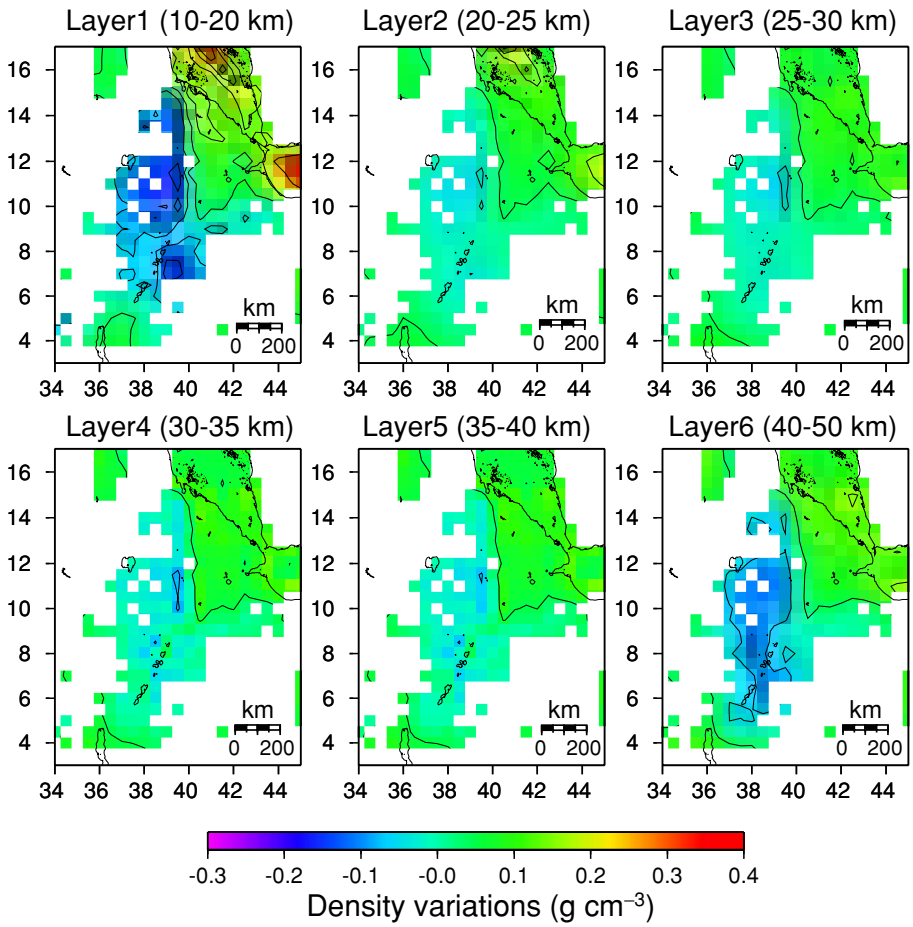

Figure 8. 3-D density distribution within each of the six layers resulting from the second inversion. Note the low density contrast (*ca.* −0.15 g cm^{-3}) crossing the MER in the last layer (z = 40–50 km) around 39°E, 7°N. The effect of high standard errors in layer 1 and 2, and low standard errors in layers 3–6 for the Red Sea and Gulf of Aden results in the concentration of high density anomaly in the upper part of the model.

deviations in these two locations, we allow the inversion to put higher density contrast at the ridge axis in the two first layers. Decreasing the standard deviations for the lower layers prevents a less physically reasonable artefact appearing deeper in the model.

The resulting model after three iterations is shown in Fig. 8 for the six layers. The rms decrease is 97 per cent (from 84.9 mGal to 2.4 mGal). The results point out several strong positive and negative contrasts. First, the effect of the Red Sea and Aden ridges is strongly marked by a positive anomaly (more than +300 kg m^{-3}) between 10 and 25 km depth, as expected from the *a priori* constraints. In the northern Afar depression, a +250 kg m^{-3} density contrast is clearly shown at 10–20 km depth. The uplifted margins of the rift are marked by a strong negative density contrast (−200 kg m^{-3}) and density decrease with depth. A transversal negative contrast of 200 kg m^{-3} is observed in the deepest layer, which spans 40 and 50 km depth.

We have carried out some tests to check the stability of our inversion, and to investigate the proper location of the density contrasts with depth. We first tried to put the *a priori* information in different layers. The standard deviation initially set to 0.1 in the layers 1 and 2 for the Red Sea and Gulf of Aden ridges were moved to layers 2 and 3 (test 1), then to layers 3 and 4 (test 2), respectively. The final rms decrease is of the same order for both tests (about 97 per cent). The high density contrasts observed in layers 1 and 2 for the Red Sea and Gulf of Aden in Fig. 8 are now localized in layers where the standard deviation is the highest, that is to say 2 and 3 (test 1) and 3 and 4 (test 2). Their amplitude is much higher because of their deeper location (+700 kg m^{-3} and +800 kg m^{-3} for test 1 and 2, respectively). As a consequence, the amplitudes of the low-density bodies increase a little, but they are localized in the same places. Their maxima are located in layer 1 beneath the western and eastern Ethiopian Plateaux, and in layer 6 transverse to the rift axis (Fig. 8).

We have also tested different numbers of layers. When taking a model shallower than 50 km (e.g. from 10 to 40 km depth), the low transverse density anomaly observed in layer 6 in Fig. 8 is blurred through all the layers. When taking a model deeper than 50 km (by adding an extra layer from 50 to 60 km depth), the same anomaly is only concentrated in the two last layers, between 40 and 60 km depth, with a decreasing amplitude. We interpret this behaviour together with the receiver function analysis by the fact that an anomalous body is present near 39°W and 7°N, and that it is most likely located in the bottom part of our models, probably below 35 km, consistent with the seismic tomography studies of Bastow *et al.* (2005).

Forward modelling

A final way to test our results is to construct a gravity model derived from our gravity inversions and seismic estimates of crustal thickness that fits unfiltered Bouguer gravity anomalies. We directly

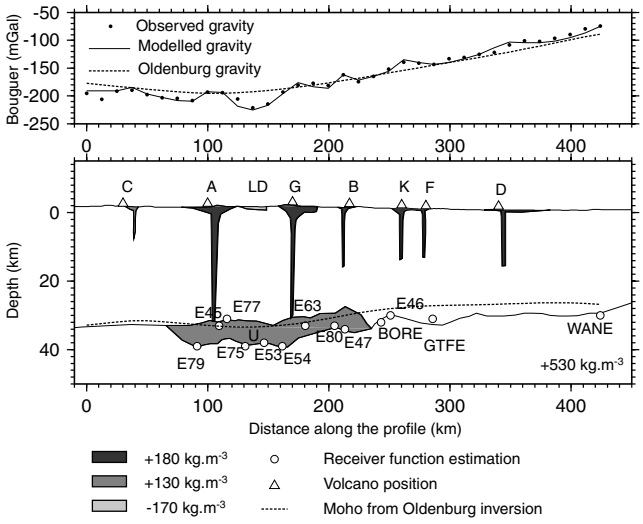

Figure 9. Model and predicted Bouguer anomaly data along profile LL′ (Fig. 6). Circles represent the Moho depth estimate from receiver functions. Triangles represent Quaternary shield volcanoes or large calderas (C = Corbetti; A = Aluto; G = Gedemsa; B = Boset; K = Kone; F = Fantale; D = Dofen). U is magmatic underplate interpreted in this study. LD are low-density bodies interpreted as sedimentary layers. Density contrasts are relative to the crustal value. Also indicated is the Moho estimation from Oldenburg inversion (dotted line in the bottom panel), and its respective gravity signal (dotted line in the upper panel). One can show that the crustal thickness rather well explains the long wavelength of gravity, whereas the shorter wavelengths are to be modelled by intrusive bodies.

model gravity anomalies with the GM-SYS Geosoft software on a profile LL′ that runs along the rift axis (Figs 6 and 9). We use the complete Bouguer anomaly from point data shown in Fig. 2, and we constrain our model with Moho depths estimated from receiver function analyses for 13 seismological stations, including WANE from Dugda *et al.* (2005) (Figs 2 and 3). The aligned chains of Quaternary eruptive centres in the magmatic segments are characterized by short-wavelength, positive Bouguer gravity anomalies (e.g. Mahatsente *et al.* 1999) (e.g. Figs 4a–d). Following the suggestions of Keranen *et al.* (2004) and Ebinger & Casey (2001) we include mafic intrusions that feed magma reservoirs and dike intrusion zones in the shallow upper crust. In our forward models, we make no attempt to determine the width or depth extent of the intrusive bodies; our aim is to test the crustal thickness estimates derived from inverse models of gravity data. As our model is only 2-D, it does not prevail on any extension or variation perpendicular to this axis. By assuming an infinite size for the body in the direction perpendicular to LL′, we minimized the section of the bodies required to explain the shortest wavelength features. Fig. 9 could be regarded as a lower bound for the section of the bodies.

The resulting 2-D model is shown Fig. 9, which shows a south to north decrease in crustal thickness, with a zone of thicker crust between E79 and E47. The long wavelength component of the signal can be well explained by a Moho discontinuity that runs through the receiver function maximum depth. The signal of the high-density bodies beneath the large eruptive centres is superposed on the regional signal emanating from crustal thickness variations; these areas may also be underplated. A shallow, low-density body (LD on Fig. 9) is included between Aluto and Gedemsa volcanoes to simulate the effect of 600 m of lacustrine and volcaniclastic strata contained in the caldera lakes (LeTurdu *et al.* 1999); these low-density bodies may account for local variations in gravity anomalies. The forward model explains both the seismic and inverse model estimates of crustal thickness variations along the length of the rift system, validating our interpretations, with the addition of shallow crustal features to explain short wavelength features not present in the filtered data.

DISCUSSION

The above Oldenburg and 3-D inversions alone are unable to precisely locate the anomalies with depth, even if we could assume after our tests that the low density transverse to the rift at 39°W and 7°N is deep and should correspond to a lower crustal body. To go further in the interpretation, we require more information which we can extract from the receiver function results.

Receiver functions show the thickest crust along the axial profile lies at 8°N, 39°E, but this thickening is seen only in the 3-D density model. The zone of locally thicker crust may be too short a wavelength to be seen in the Oldenburg solution (stations AMME, E54, E53, E75, E79). From the 3-D density model we retrieve deep, low-density sources at this location (layer 6, Fig. 8). The direction of this perturbation is transverse to the main rift axis, and correlates very well with a deep interface retrieved by the receiver functions and seismic refraction data (Maguire *et al.* 2003). We are fully aware that this kind of 3-D inversion is not well enough constrained to be unique. The fact that this result is seen in a totally independent data set, however, advocates its close approximation to the structure of the Ethiopian plateau and superposed rift valleys. Its low density value (*ca.* -150 kg m^{-3}) compared to the background mantle value (layer 6, Fig. 8) and its location argue for an underplated crust.

Calibration of our results with independent seismic data allows us to map crustal thickness variations across the region, and examine the effects of magmatism and rifting on crustal structure. The comparison between the inversion for crustal thickness, 3-D gravity inversion and receiver function results shows the following principal features, which provide insights into modification of continental lithosphere by plume and continental breakup processes.

(1) Thin crust is predicted beneath the magmatic segments (axial volcanic ranges) in the northern Afar depression (Figs 1 and 4a). The low, broad form of Erta ‘Ale and its persistent lava lake suggest that it forms largely through intrusion, and functions as an incipient slow-spreading mid-ocean ridge (Oppenheimer & Francis 1997). In light of these observations, we interpret the inversion results as a combination of crustal thinning and a lateral increase in density corresponding to magmatic intrusions feeding the volcanic chains. Assuming each end member, we obtain a minimum crustal thickness of 23 km (no lateral density contrast), or a density contrast of 240 kg m^{-3} (with no thinning).

(2) A shallower Moho is found along the rift axis, with crustal thickness values decreasing from 32 to 33 km in the south to 24 km beneath southern Afar. These estimates concur with across and along-axis seismic refraction profiles (Maguire *et al.* 2003; Keller *et al.* 2004; Mackenzie *et al.* 2005) and receiver function estimates of crustal thickness beneath the rift zone (Fig. 6). From our gravity analyses, no significant crustal density signature or crustal thickness variation is observed within the Afar depression. There are no profound changes from north to south, despite the complex tectonic history within a migrating triple junction zone (e.g. Eagles *et al.* 2002; Manighetti *et al.* 2001). There may be, however, smaller-scale variations at wavelengths excluded from our analyses.

(3) Crustal thickness predicted in the inversions increases to more than 40 km beneath the ∼2500-m-high Ethiopian plateau

flanking the southern Red Sea margins, consistent with receiver function estimates of crustal thickness (Fig. 6). Our inversions underpredict crustal thickness on the plateau because the inversion does not take into account the higher density of the underplate. The thickest crust corresponds to the region of thickest Oligocene flood basalts, which crop out along the southwestern margin of the southern Red Sea. There is an apparent asymmetry across the MER, with thinner crust predicted beneath the southeastern side of the MER (Somali plate) than on the northeastern side (Nubia plate) (Fig. 6). This asymmetry has been noted in teleseismic delay times, which decrease to the south and are interpreted as thinner, higher velocity crust and upper mantle (Bastow *et al.* 2005). The coincidence of thick extrusive volcanic piles and thicker crust suggest that the locus of magmatic underplating coincides with the margins of the ∼28 Ma southern Red Sea rift, which terminated at ∼10°N until linkage with the MER was achieved at ∼10 Ma (Wolfenden *et al.* 2004, 2005).

These crustal thickness variations have implications for evolution of the Oligocene plume province. The 1.5 to 2 km-thick flood basalts act as a load on the plate, partially countering the buoyancy effects of underplating and hot mantle. Thus, stripping off the effects of the volcanic leads to ∼70 m of uplift above the mean plateau elevation, assuming 2800 kg m^{-3} basalt layer. Assuming Airy isostatic compensation for the crustal thickness variations observed throughout the study region, a mean crustal density of 2700 kg m^{-3}, an upper mantle density of 3200 kg m^{-3}, and a compensating root of 14 km relative to the 28-km-thick crust outside the flood basalt province provides an estimate of 2.5 km of plateau uplift. Thus, our combined interpretation of gravity and seismic data indicates that most of the plateau uplift is isostatically compensated by magmatic underplating, most of which is probably associated with the ∼31–29 Ma flood basalt event along the southern Red Sea region. Given the variation in underplate thickness estimates and possible errors in pre-rift crustal thickness, there may be a few hundred metres of dynamic uplift from a plume tail, which may now be south of the study area (e.g. Ebinger & Sleep 1998), or beneath the Afar depression (e.g. Montelli *et al.* 2004).

(4) A girdle of thicker crust underlies the MER valley in the region of the lakes, which fill faulted calderas (Fig. 6). The crust is either thicker (40 km from the receiver function analysis) or less dense (−150 kg m^{-3}). This can reflect either a segmentation in the rift structure or a considerable thickness of magmatic underplate beneath the surface expression of explosive volcanism. The less extended southern rift sector also lacks magmatic segments, suggesting that higher levels of magmatic intrusion accompany magmatic segment development.

Our estimates of crustal thickness differ considerably with patterns predicted in the 3-D forward models of Mahatsente *et al.* (1999), who predict a decrease in crustal thickness southward along the MER, and a greater crustal thickness beneath the southeastern flank than the northwestern rift flank. Some of these differences may be caused by the limited size of their study region, as well as differences in model assumptions.

New and existing data document significant along-axis variations in the amount of crustal stretching, and provide information on magmatic intrusion and underplating of the crust beneath the flood basalt province. Rifting commenced concurrent with or immediately after the flood basalt episode, so we reference crustal stretching to the 40-km-thick crust beneath the plateau. Assuming that this crustal thickness is the one before MER extension (i.e. at ∼11 Ma), and considering the crustal thickness we obtain in this study, the crustal stretching factor β is ∼2 within the Afar depression from WANE north, but is ∼1.2 in the central MER (Fig. 6). Clearly, these are minimum stretching estimates considering the seismic evidence for underplating and intrusion beneath magmatic segments. The station WANE is located near the palaeotriple junction, north of which crust has experienced a longer stretching and magmatic history.

CONCLUSIONS

Gravity data inversions constrained by seismic data allow us to map crustal thickness and/or density variations across the uplifted and rifted Cenozoic flood basalt province. Inversion results for the rift valleys and supporting seismic data indicate that the faulted and volcanically active Main Ethiopian, southern Red Sea, and easternmost Gulf of Aden rift valleys are underlain by thinner, denser crust than underlies the adjacent plateaux. Crustal thickness decreases from south to north along the length of the MER, with a sharp decrease into the Afar depression. Forward and inverse models predict a lens of underplate beneath the rift south of ∼8°N; this layer is absent in rift sectors with magmatic segments. Crustal thickness beneath the uplifted Ethiopian plateau along the southern Red Sea margin (Nubian plate) is >40 km, consistent with receiver function estimates of crustal thickness (44 km) and seismic refraction data. These estimates indicate that almost the entire part of the 2.5 km plateau uplift is isostatically supported by crustal thickness variations, and magmatic underplating.

Our inverse models and their comparisons with forward models and seismic data document indicate that the crust beneath the uplifted plateau and the rift valleys has been modified by magmatic underplating and intrusion. Crust beneath the rifts has been stretched, with amount of stretching increasing from south to north into the Afar depression. Within the southern Red Sea rift where seismic constraints are few and rifting has occurred over a longer time period, our estimates of crustal thinning may be overestimates. Thus, magmatic processes prior to and during rifting have fundamentally changed the density structure of the crust prior to continental breakup.

ACKNOWLEDGMENTS

Many thanks to Olivia, Côme, Lysandre, Adèle and Antonin, for their welcome interruptions. Ketema Tadesse, Abiy Hunegnaw, Moges Tegabe and Ketsela Tadesse are thanked for providing access to Geological Survey of Ethiopia gravity data. We thank Eve Daly for her careful review. Hélène Hébert is greatly thanked for providing us the Tadjoura-Aden gravity data. We would like also to thank R. Holme, M. Kaban and an anonymous reviewer for their helpful suggestions to improve this manuscript. Almost all figures were prepared with the Generic Mapping Tool developed by P. Wessel and W. Smith (1995). CT acknowledges a Marie Curie post-doctoral felloswhip HPMF-CT-2000-00630. CE is grateful for support from the Leverhulme Trust and NERC grant NER/T/S/2000/00647. This is IPGP contribution n° 2080.

REFERENCES

Ayalew, D. & Yirgu, G., 2003. Crustal contribution to the genesis of Ethiopian plateau rhyolitic ignimbrites: basalt and rhyolite geochemical provinciality, *J. geol. Soc. Lond.,* **160,** 47–56.

Ayalew, D., Bourdon, E., Ebinger, C., Wolfenden, E. & Yirgu, G., 2005. Temporal compositional variation of early syn-rift rhyolites along the western Red Sea margin and northern Main Ethiopian rift, submitted to Yirgu, G.,

Ebinger, C., and Maguire, P., Structure and dynamics of the East African rift system in the Afar volcanic province, *Geol. Soc. London Spec. Pub.*, submitted.

Ayele, A., Stuart, G. & Kendall, J.M., 2004. Insights into rifting from shear-wave splitting in press: an example from Ethiopia, *Geophys. J. Int.,* **157,** 354–362.

Barberi, F. & Varet, J., 1977. Volcanism of Afar: Small-scale plate tectonic implications, *Bull. geol. Soc. Am.,* **56,** 903–915.

Bastow, I.D., Stuart, G.W., Kendall, J.-M. & Ebinger, C.J., 2005. Upper-mantle seismic structure in a region of incipient continental breakup: northern Ethiopian rift, *Geophys. J. Int.,* **162,** 479–493.

Bellahsen, N., Faccenna, C., Funiciello, F., Daniel, J.M. & Jolivet, L., 2003. Why did Arabia separate from Africa? Insights from 3-D laboratory experiments, *Earth planet. Sci. Lett.,* **216,** 365–381.

Benoit, M.H., Nyblade, A.A., VanDecar, J.C. & Gurrola, H., 2003. Upper mantle P wave velocity structure and transition zone thickness beneath the Arabian Shield, *Geophys. Res. Lett.,* **30,** 1531, doi:10.1029/2002GL016436.

Berckhemer, H. *et al.*, 1975. Deep seismic soundings in the Afar region and on the highland of Ethiopia, in *Afar Between Continental and Oceanic Rifting,* pp. 89–107, eds. Pilger, A. & Rösler, A., Schweizerbart Stuttgart.

Bosellini, A., Russo, A. & Assefa, G., 2001. The Mesozoic succession of Dire Dawa, Harar province, Ethiopia, *J. Afri. Earth Sci.,* **32,** 403–417.

Boutilier, R. & Keen, C., 1999. Small-scale convection and divergent plate boundaries, *J. geophys. Res.,* **104,** 7389–7403.

Buck, W.R., 2004. Consequences of athenospheric variability on continental rifting, in *Rheology and Deformation of the Lithosphere at Continental Margins,* pp. 1–30, eds. Karner, G.D., Taylor, B., Driscoll, N. & Kohlstedt, D., Columbia University Press, New York.

Christensen, N. & Mooney, W., 1995. Seismic velocity structure and composition of the continental crust: a global view, *J. Geophys. Res.,* **100,** 9761–9788.

Cochran, J.R., 1981. The Gulf of Aden: structure and evolution of a young ocean basin and continental margin, *J. geophys. Res.,* **86,** 263–288.

Cochran, J.R., 1983. A model for development of the Red Sea, *AAPG Bull.,* **67,** 41–69.

Coffin, M. & Eldholm, O., 1994. Large igneous provinces: crustal structure, dimensions, and external consequences, *Rev. Geophys.,* **32,** 1–36.

Courtillot, V., Davaille, A., Besse, J. & Stock, J., 2003. Three distinct types of hotspots in the Earth's mantle, *Earth planet. Sci. Lett.,* **205,** 295–308.

Cox, K., 1980. A model for flood basalt volcanism, *J. Petrol.,* **21,** 629–650.

Daly, E., Keir, D., Ebinger, C. & Stuart, G., 2005, Along-axis segmentation of a transitional continental rift from crustal tomography studies in Ethiopia, submitted to *J. geophys. Res.*, submitted.

Dugda, M., Nyblade, A., Julia, J., Langston, C.A., Ammon, C. & Simiyu, S., 2005. Crustal structure in Ethiopia and Kenya from receiver function analyses: Implication for rift development in eastern Africa, *J. geophys. Res.,* **110,** B01303, doi:10.1029/2004JB003065.

Eagles, G., Gloaguen, R. & Ebinger, C., 2002. A model for the creation of a microplate: kinematics of the Danakil microplate, *Earth planet. Sci. Lett.,* **203,** 607–620.

Ebinger, C.J. & Hayward, N., 1996. Soft plates and hot spots: Constraints from the Ethiopian and Afar rifts, *J. geophys. Res.,* **101,** 21 859–21 876.

Ebinger, C.J. & Sleep, N.H., 1998. Cenozoic magmatism in central and east Africa resulting from impact of one large plume, *Nature,* **395,** 788–791.

Ebinger, C.J. & Casey, M., 2001. Continental breakup in magmatic provinces: an Ethiopian example, *Geology,* **29,** 527–530.

Ebinger, C., Bechtel, T., Forsyth, D. & Bowin C., 1989. Effective elastic plate thickness beneath the East-African and Afar plateaus and dynamic compensation of the uplifts, *J. geophys. Res.,* **94,** 2883–2901.

Ebinger, C.J., Yemane, T., WoldeGabriel, G., Aronson, J.L. & Walter R.C., 1993. Late Eocene–Recent volcanism and faulting in the southern main Ethiopian rift, *J. geol. Soc. Lond.,* **150,** 99–108.

George, R., Rogers, N. & Kelly, S., 1998. Earliest magmatism in Ethiopia: Evidence for two mantle plumes in one flood basalt province, *Geology,* **26,** 923–926.

Ghebreab, W. & Talbot, C., 2000. Red Sea extension influenced by Pan-African tectonic grain in eastern Eritrea, *J. Struc. Geology,* **22,** 931–946.

Hadiouche, O., Jobert, N. & Montagner, J.-P., 1989. Anisotropy of the African continent inferred from surface waves, *Phys. Earth planet. Int.,* **58,** 61–81.

Hayward, N. & Ebinger, C.J., 1996. Variations in along-axis segmentation of the Afar Rift System, *Tectonics,* **15,** 244–257.

Hébert, H., Deplus, C., Huchon, P. & Khanbari, K., 2001. Lithospheric structure of a nascent spreading ridge inferred from gravity data: the western Gulf of Aden, *J. geophys. Res.,* **106,** 26 345–26 364.

Hebert, L. & Langston, C.A., 1985. Crustal thickness estimates at AAE and NAI using teleseismic P-wave conversions, *Tectonophysics,* **111,** 299–327.

Hofmann, C., Courtillot, V., Féraud, G., Rochette, P., Yirgu, G., Ketefo, E. & Pik, R., 1997. Timing of the Ethiopian flood basalt event and implications for plume birth and global change, *Nature,* **389,** 838–841.

Holbrook, W.S. & Kelemen, P., 1993. Large igneous province on the US Atlantic margin and implications for magmatism during continental breakup, *Nature,* **364,** 433–436.

Keller, G.R., Harder, S.H., O'Reilly, B., Mickus, K., Tadesse, K., Maguire, P.K.M. & the EAGLE Working Group, 2004. A preliminary analysis of crustal structure variations along the Ethiopian Rift, in Yirgu, G. *et al.*, eds, *Proceedings of the International Conference on the East African Rift System, June 20–24, 2004, Addis Ababa, Ethiopia,* Ethiopian Geoscience and Mineral Engineering Association, pp. 97–101.

Kendall, J.-M., Stuart, G., Ebinger, C., Bastow, I. & Keir, D., 2005. Magma-assisted rifting in Ethiopia, *Nature,* **433,** 146–148.

Keranen, K., Klemperer, S., Gloaguen, R. & EAGLE Working Group, 2004. Three-dimensional seismic imaging of a protoridge axis in the Main Ethiopian rift, *Geology,* **32,** 949—952.

Kieffer, B. *et al.*, 2004. Flood and shield basalts from Ethiopia: Magmas from the African Superswell, *J. Petrol.,* **45,** 793—834.

King, S. & Anderson, D., 1998. Edge-driven convection, *Earth planet. Sci. Lett.,* **160,** 289–296.

Knox, R., Nyblade, A. & Langston, C., 1998. Upper mantle S wave velocities beneath Afar and western Saudi Arabia from Rayleigh wave dispersion, *Geophys. Res. Lett.,* **25,** 4233–4236.

Korenaga, J., Holbrook, W.S., Kent, G.M., Keleman, P.B., Detrick, R.S., Larsen, H-C., Hopper, J.R. & Dahl-Jensen, T., 2000. Crustal structure of the southeast Greenland margin from joint refraction and reflection seismic tomography, *J. geophys. Res.,* **105,** 21 591–21 614.

LeTurdu, C. *et al.*, 1999. The Ziway-Shala lake basin system, Main Ethiopian rift: influence of volcanism, tectonics, and climatic forcing on basin formation and sedimentation, *Palaeo.,* **150,** 135–177.

Mackenzie, G.D., Thybo, H. & Maguire, P.K.H., 2005. Crustal velocity structure across the Main Ethiopian Rift: Results from two-dimensional wide-angle seismic modelling, *Geophys. J. Int.,* **162,** 994–1006.

Maguire, P. *et al.*, 2003. Geophysical project in Ethiopia studies continental breakup, *EOS, Trans. Am. geophys. Un.,* **84,** 337–340.

Mahatsente, R., Jentzsch, G. & Jahr, T., 1999. Crustal structure of the Main Ethiopian rift from gravity data: 3-dimensional modelling, *Tectonophysics,* **313,** 363–382.

Makris, J. & Ginzburg, A., 1987. The transition between continental rifting and sea-floor spreading, *Tectonophysics,* **141,** 199–214.

Manighetti, I., Tapponnier, P., Courtillot, V., Gruszow, S. & Gillot, P.-Y., 1997. Propagation of rifting into along the Arabia-Somalia plate boundary: the Gulfs of Aden and Tadjurah, *J. geophys. Res.,* **102,** 2681–2710.

Manighetti, I., Tapponnier, P., Courtillot, V., Gallet, Y., Jacques, E. & Gillot, P.-Y., 2001. Strain transfer between disconnected, propagating rifts in Afar, *J. geophys. Res.,* **106,** 13 613–13 666.

Mechie, J. & Prodehl, C., 1988. Crustal and uppermost mantle structure beneath the Afro-Arabian Rift System, *Tectonophysics,* **153,** 103–121.

Menzies, M., Klemperer, S., Ebinger, C. & Baker, J., 2002. Characteristics of volcanic rifted margins, volcanic rifted margins, *Geol. Soc. Am. Spec.* Pap. 362.

Mohr, P., 1989. Nature of the crust under Afar—New igneous not thinned continental, *Tectonophysics,* **167,** 1–11.

Montelli, R., Nolet, G., Dahlen, F.A., Masters, G., Engdahl, E.R. & Hung, S.-H., 2004. Finite-frequency tomography reveals a variety of plumes in the mantle, *Science,* **303,** 338–343.

Oldenburg, D.W., 1974. The inversion and interpretation of gravity anomalies, *geophysics,* **39,** 526–536.

Oppenheimer, C. & Francis, P., 1997. Remote sensing of heat, lava, and fumarole emissions fomr Erta 'Ale volcano, Ethiopia, *Int. J. Remote Sens.,* **18,** 1661–1692.

Parker, R.L., 1972. The rapid calculation of potential anomalies, *Geophys. J. R. astr. Soc.,* **31,** 447—455.

Pik, R., Marty, B., Carignan, J. & Lavé, J., 2003. Stability of the upper Nile drainage network (Ethiopia) deduced from (U-Th)/He thermochronometry: implications for uplift and erosion of the Afar plume dome, *Earth planet. Sci. Lett.,* **215,** 73–88.

Ritsema, J. & van Heijst, H., 2000. A new model for the upper mantle structure beneath Africa, *Geology,* **28,** 63–66.

Stuart, G., Bastow, I. & Ebinger, C., 2005. Crustal structure of the northern Main Ethiopian rift from receiver function studies, submitted to Yirgu, G., Ebinger, C., and Maguire, P., Structure and dynamics of the East African rift system in the Afar volcanic province, *Geol. Soc. London Spec. Pub.*, submitted.

Tesfaye, S., Kusky, T.T. & Harding, D., 2003. Early Continental breakup boundary and migration of the Afar triple junction, Ethiopia, *Geol. Soc. Am. Bull.,* **115,** 1053–1067.

Wessel, P. & Smith, W.H.F., 1991. Free software helps map and display data, *EOS Trans. Am. Geophys. Um.,* **72,** 445–446.

White, R. & McKenzie, D., 1989. Magmatism at rift zones: The generation of volcanic continental margins and flood basalts, *J. Geol. Res.,* **94,** 7685–7729.

Widiwijayanti, C., Tiberi, C., Deplus, C., Diament, D., Mikhailov, V. & Louat, R., 2004. Geodynamic evolution of the northern Molucca Sea area (eastern Indonesia) constrained by 3-D gravity field inversion, *Tectonophysics,* **386,** 203–222.

WoldeGabriel, G., Aronson, J.L. & Walter, R.C., 1990. Geology, geochronology and rift basin development in the central sector of the Main Ethiopian Rift, *Geol. Soc. Am. Bull.,* **102,** 439–485.

Woldetinsae, G. & Götze, H-J., 2005. Gravity field and isostatic state of Ethiopia and its adjacent areas, *J. Afri. Earth Sciences,* **41,** 103–117.

Wolfenden, E., Yirgu, G., Ebinger, C., Ayalew, D. & Deino, A., 2004. Evolution of the northern Main Ethiopian rift: birth of a triple junction, *Earth planet. Sci. Lett.,* **224,** 213–228.

Wolfenden, E., Ebinger, C., Yirgu, G., Renne, P. & Kelley, S.P., 2005. Evolution of a volcanic rifted margin: Southern Red Sea, Ethiopia, *Geol. Soc. Am. Bull,* **117,** 846–864.